Opto-Electronic Advances

ISSN 2096-4579 CN 51-1781/TN

Three-dimensional isotropic microfabrication in glass using spatiotemporal focusing of high-repetition-rate femtosecond laser pulses

Yuanxin Tan, Haotian Lv, Jian Xu, Aodong Zhang, Yunpeng Song, Jianping Yu, Wei Chen, Yuexin Wan, Zhaoxiang Liu, Zhaohui Liu, Jia Qi, Yangjian Cai and Ya Cheng

Citation: Tan YX, Lv HT, Xu J, Zhang AD, Song YP et al. Three-dimensional isotropic microfabrication in glass using spatiotemporal focusing of high-repetition-rate femtosecond laser pulses. *Opto-Electron Adv* **6**, 230066(2023).

https://doi.org/10.29026/oea.2023.230066

Received: 24 April 2023; Accepted: 20 July 2023; Published online: 15 September 2023

Opto-Electronic Advances

Article

October 2023, Vol. 6, No. 10

DOI: 10.29026/oea.2023.230066

Three-dimensional isotropic microfabrication in glass using spatiotemporal focusing of high-repetition-rate femtosecond laser pulses

Yuanxin Tan[1,3,4], Haotian Lv[1], Jian Xu[2*], Aodong Zhang[2], Yunpeng Song[2], Jianping Yu[2], Wei Chen[2], Yuexin Wan[2], Zhaoxiang Liu[2], Zhaohui Liu[2], Jia Qi[2], Yangjian Cai[1,3,4*] and Ya Cheng[2,3*]

To improve the processing efficiency and extend the tuning range of 3D isotropic fabrication, we apply the simultaneous spatiotemporal focusing (SSTF) technique to a high-repetition-rate femtosecond (fs) fiber laser system. In the SSTF scheme, we propose a pulse compensation scheme for the fiber laser with a narrow spectral bandwidth by building an extra-cavity pulse stretcher. We further demonstrate truly 3D isotropic microfabrication in photosensitive glass with a tunable resolution ranging from 8 μm to 22 μm using the SSTF of fs laser pulses. Moreover, we systematically investigate the influences of pulse energy, writing speed, processing depth, and spherical aberration on the fabrication resolution. As a proof-of-concept demonstration, the SSTF scheme was further employed for the fs laser-assisted etching of complicated glass microfluidic structures with 3D uniform sizes. The developed technique can be extended to many applications such as advanced photonics, 3D biomimetic printing, micro-electromechanical systems, and lab-on-a-chips.

Keywords: simultaneous spatiotemporal focusing technique; pulse compensation; pulse stretcher; 3D isotropic fabrication; chemical etching

Tan YX, Lv HT, Xu J, Zhang AD, Song YP et al. Three-dimensional isotropic microfabrication in glass using spatiotemporal focusing of high-repetition-rate femtosecond laser pulses. *Opto-Electron Adv* **6**, 230066 (2023).

Introduction

Femtosecond (fs) laser direct writing (FLDW) in transparent materials, as a powerful three-dimensional (3D) microfabrication technology based on nonlinear laser-material interaction, has exhibited broad and promising applications in many fields such as micro/nanophotonics, integrated optics, microfluidics, and optofluidics[1–11]. For instance, FLDW can be applied to fabricate 3D optical waveguides in various transparent dielectrics[12,13], Bragg gratings in fibers[14], microfluidic and optofluidic structures[15], and proteinaceous micro/nanostructures[16]. Although significant advances have been made in

[1]Shandong Provincial Engineering and Technical Center of Light Manipulations & Shandong Provincial Key Laboratory of Optics and Photonic Device, School of Physics and Electronics, Shandong Normal University, Jinan 250014, China; [2]XXL—The Extreme Optoelectromechanics Laboratory, School of Physics and Electronics Science, East China Normal University, Shanghai 200241, China; [3]Joint Research Center of Light Manipulation Science and Photonic Integrated Chip of East China Normal University and Shandong Normal University, East China Normal University, Shanghai 200241, China; [4]Collaborative Innovation Center of Light Manipulation and Applications, Shandong Normal University, Jinan 250358, China.

*Correspondence: J Xu, E-mail: jxu@phy.ecnu.edu.cn; YJ Cai, E-mail: yangjiancai@sdnu.edu.cn; Y Cheng, E-mail: ya.cheng@siom.ac.cn

Received: 24 April 2023; Accepted: 20 July 2023; Published online: 15 September 2023

micro/nanostructure fabrication and functional device application using the FLDW, it is still a challenge to maintain the 3D isotropic processing resolution during the fabrication of arbitrary-shaped microstructures. Typically, the focal spot produced by FLDW has an asymmetrical shape and the axial resolution is significantly elongated, which inherently limits the 3D fabrication homogeneity of FLDW. To balance the differences between the lateral and axial resolutions of FLDW, several beam shaping techniques have been proposed[17–21], such as slit shaping[17,18], astigmatic shaping[19], and crossed beam irradiation[20]. However, these techniques cannot achieve 3D isotropic fabrication based on a single objective lens.

As a unique ultrafast laser beam shaping technique, the simultaneous spatiotemporal focusing (SSTF) technique was originally developed for bio-imaging applications[22,23], and has been applied in fs laser micromachining[24–34]. The SSTF technique provides a new temporal focusing dimension, making it prominent in improving the axial fabrication resolution[24–27], eliminating the nonlinear self-focusing[28,29], and increasing the fabrication efficiency[30,31]. The mechanism of the SSTF technique is that different frequency components of fs laser pulses are spatially dispersed by gratings and then recombined by an objective lens. With the SSTF technique, embedded microfluidic channels with circular cross-sections in silica glass were fabricated using the laser assisted etching[24] and high aspect-ratio channels were processed in thick silica glass using laser backside machining[25]. In our previous work[30], a 3D isotropic fabrication resolution of ~85 μm was achieved in glass using the SSTF scheme. However, these results are all achieved by using Ti: sapphire chirped pulse amplification system with a central wavelength of 800 nm, wide spectral bandwidth (~30 nm), and low repetition frequency (1 kHz). Notably, a wide spectral bandwidth is beneficial for spatial dispersion and pulse compensation in the SSTF scheme, but the relatively low repetition rate limits the fabrication speed. Moreover, exploring the possibility of 3D isotropic fabrication with a tunable resolution in glass has yet not been studied.

To improve the fabrication speed and extend the processing window of 3D isotropic microfabrication, the use of fs fiber laser amplification systems with high repetition rates is highly desirable. However, high-repetition-rate fs fiber laser sources usually could not provide a sufficient pulse compensation for the SSTF scheme due to their narrow spectral bandwidths which limits the application of SSTF technique on those systems.

To overcome this problem, we propose a pulse compensation scheme by building a pulse stretcher outside a high-repetition-rate fs fiber laser source for the generation of the SSTF fs laser pulses. Further, we demonstrate truly 3D isotropic microfabrication in glass with a tunable resolution ranging from 8 μm to 22 μm. Then, we systematically investigated the influences of pulse energy, speed, depth, and spherical aberration on fabrication resolution. Finally, SSTF FLDW followed by chemical etching was employed for demonstration of the processing capability of 3D complicated and spatially homogenous microfluidic structures in Foturan glass[6,35,36]. Compared with previous SSTF works, the proposed technique extends the SSTF scheme to a high repetition rate and narrow bandwidth fs fiber laser source, which not only improves the fabrication efficiency of FLDW but also extends the tunable range of 3D isotropic fabrication resolution.

Experimental setup

Figure 1 shows the schematic of the experimental layout for the SSTF micromachining system. The laser source is an ultrashort pulsed fiber laser amplifier system (Light Conversion, Carbide 30 W) with a center wavelength of 1030 nm, a variable pulse duration ranging from 250 fs to 10 ps, and a variable repetition rate ranging from 1 kHz to 1 MHz. The pulse energy can be controlled by setting the transmission rate of the laser source and the output laser beam has a nearly perfect Gaussian shape with a ~3 mm diameter.

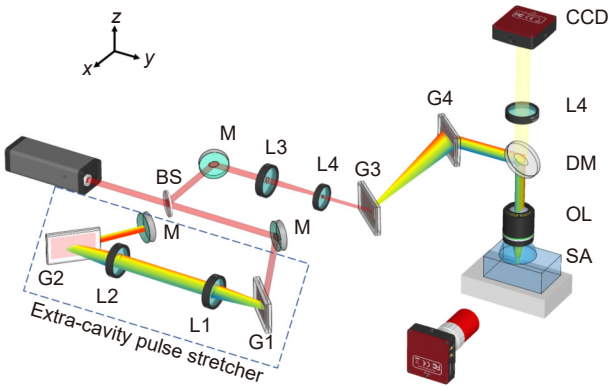

Fig. 1 | Schematic of the experimental layout. BS: beam splitter; M: mirror; G1–G4: diffraction gratings; L1–L4: lenses with different focal lengths; DM: dichroic mirror; OL: objective lens; SA: sample. The dashed rectangle indicates the proposed extra-cavity pulse stretcher.

In the SSTF scheme, different frequency components are separated from each other in space by a single-pass grating compressor. It should be noted that the spectral bandwidth of the high-repetition-rate fiber laser system is only ~8 nm, which is smaller than the typical spectral bandwidth of Ti: saphirre chirped pulse amplification system. Such a high-repetition-rate fs laser with a narrow spectral bandwidth needs more angular chirp rate to obtain sufficient spatial dispersion, which also directly introduces a large number of negative Group Delay Dispersion (GDD). However, the large number of negative GDD cannot be compensated by tuning the laser source itself.

To simultaneously obtain sufficient spatial dispersion and compensation for the temporal chirp, we built an extra-cavity pulse stretcher to provide positive temporal chirps, as illustrated in Fig. 1. A Martinez-type pulse stretcher was adopted to introduce a large number of positive temporal chirps[37], which consist of a double-pass configuration with the gratings (G1 and G2) at the Littrow angle and a telescope system (L1 and L2). The incident angles of both transmission gratings (Gitterwerk, 1739 lines/mm, blazing at 1030 nm) were all 63.6°, the focal lengths of two convex lenses L1 and L2 were all 150 mm, the distance between the lens was 300 mm and the distance between the grating and convex lens was ~116 mm. The effective distance of the pulse stretcher z was estimated to be ~136 mm.

The GDD introduced by the pulse stretcher can be expressed as

$$GDD = \frac{\mathrm{d}^2\phi}{\mathrm{d}\omega^2} = \frac{\lambda^3 z}{2\pi c^2\sigma^2\cos^2\theta}\,, \tag{1}$$

where z is the effective distance of the stretcher, σ is the grating constant, and θ is the first-order diffraction angle. The GDD introduced by the pulse stretcher in this experiment was estimated to be ~4.0107×10^6 fs^2, and the output pulse width was stretched to be ~45.789 ps after passing through the pulse stretcher.

To obtain a stronger spatiotemporal coupling effect in the SSTF scheme, a telescope system consisting of a convex lens L3 (f = 300 mm) and a concave lens L4 (f = −100 mm) was employed to reduce the beam diameter to ~1 mm (1/e^2). The laser beam was then directed through the single-pass grating compressor, which consists of two transmission gratings (G3 and G4, Gitterwerk, 1379 lines/mm, blazing at 1030 nm). The incident angle of the gratings was 45° and the distance between the gratings was ~410 mm. It should be noted that the single-pass grating compressor in the SSTF scheme had two main purposes. On the one hand, the grating compressor introduces proper spatial dispersion, with the grating distance of 410 mm, all the frequency components can fill the pupil of the objective lens. On the other hand, the grating compressor can provide negative GDD, which can be used to compensate for the positive GDD induced by all optics including the pulse stretcher, lenses, and so on. The GDD introduced by the grating compressor in this experiment was estimated to be -4.3756×10^6 fs^2.

After being dispersed by the grating pair, the sizes of the laser beam were measured to be ~13 mm (1/e^2) in the chirped dimension and ~1 mm (1/e^2) in the non-chirped dimension. The spatially dispersed fs laser pulses were then focused into the glass sample using a water immersion objective lens (Olympus, 20×) with a numerical aperture (NA) of 1.0 and a working distance of 2 mm, the objective lens was immersed in water to minimize spherical aberrations. Notably, the effective NA estimated in this study was only 0.097.

To obtain the shortest pulse duration at the focus of the objective lens in the SSTF scheme, the output pulse from the amplifier should be pre-chirped by adjusting the compressor in the amplifier system. In the experiment, the strongest ionization of the air was observed at the focus of the objective lens when the output pulse duration from the amplifier system was set at −3.5 ps.

The samples used in the experiment were photosensitive glass Foturan (Schott Glass Corp), which were cut into 10 mm × 10 mm × 1.6 mm coupons with all six sides polished. The glass can be regarded as a great indicator for the microfabrication process because the laser-modified area is not visible after the laser irradiation but turns to brown after a thermal annealing process (the temperature was first increased to 500 °C at 5 °C/min and held for one hour; and then raised to 605 °C at 5 °C/min and held for one hour). The glass sample was mounted on a computer-controlled XYZ stage with a resolution of 1 μm, and the front surface of the sample was immersed in purified water. The whole fabrication process was monitored by two charge-coupled devices (CCD) cameras from the top and side, respectively.

Theoretical analysis

Theoretically, in the SSTF scheme, the normalized light field of a spatially dispersed pulse E_1 at the entrance

aperture of an objective lens can be expressed as[24,26,28].

$$E_1(x,y,\omega) = E_0 \exp\left[-\frac{(\omega-\omega_0)^2}{\Omega^2}\right] \times \exp\left\{-\frac{[x-\alpha(\omega-\omega_0)]^2+y^2}{\omega_{in}^2}\right\}, \quad (2)$$

where E_0 is the constant field amplitude, ω_0 is the carrier frequency, $2\ln 2\Omega$ is the FWHM of the frequency spectrum of the pulse, and $\alpha(\omega-\omega_0)$ is the linear shift of each spectral component. In our experiments, the spectral bandwidth was only 8 nm, and the beam waist was ω_{in} = 1 mm. According to ref.[18], the angular chirp rate

$$\alpha = d\lambda_0 \cos i/(\sigma\omega_0 \cos^3\gamma), \quad (3)$$

where d is the distance between the gratings; i and γ are the incident angle and the first-order diffractive angle, respectively; σ is the groove density of the gratings; λ_0 is the carrier wavelength. We can calculate the angular chirp rate α = 6.5635 ×10^{-16} m·s/rad in the experiment. The numerically calculated and experimental measured laser intensity distributions at the entrance aperture of the objective lens are shown in Fig. 2(a) and 2(b), respectively. The experimental results were captured by a laser beam profiler (DataRay Inc.) and the measurement plane was right near the entrance aperture of the objective lens. It is obvious that in the SSTF scheme, different frequency components are separated from each other in the X direction after passing through the grating pair, the intensity distribution of the laser beam appears to be elliptical and the spatial chirp ratio (the ratio of the spatially chirped size to the input beam diameter) in the experiment is β = 13.

After passing through the objective lens, the laser field can be calculated using the slowly varying envelope approximation, which can be written as

$$E_2(x,y,\omega) = E_1(x,y,\omega)\exp\left[-ik\frac{x^2+y^2}{2f}\right], \quad (4)$$

where k is the wave vector, and f is the focal length of the objective lens. Under the paraxial approximation, the light field near the focus can be described using the Fresnel diffraction formula, which is

$$E_3(x,y,z,\omega) = \frac{\exp(ikz)}{i\lambda z}\iint_{-\infty}^{\infty} E_2(\xi,\eta,\omega) \cdot \exp\left\{ik\frac{(x-\xi)^2+(y-\eta)^2}{2z}\right\} d\varepsilon d\eta . \quad (5)$$

By performing an inverse Fourier transform of E_3, the intensity distribution in the time domain can be written as

$$I(x,y,z,t) = |E_4(x,y,z,t)|^2 = \left|\int_{-\infty}^{\infty} E_3(x,y,z,\omega)\exp(-i\omega t)d\omega\right|^2 . \quad (6)$$

Figure 2(b–d) shows the numerically calculated spatial intensity distributions near the focus of the objective lens with the SSTF scheme in XY, YZ, and XZ plans, respectively. Figure 2(f–h) are the corresponding experimental measured intensity distributions in glass, which were captured by an optical imaging system consisting of an objective lens (Mitutoyo, 20×, the numerical aperture is 0.3) and a CCD camera. The pulse energy was set to be 8 μJ (measured before the objective lens) and the intensity distributions were recorded 300 μm beneath the glass surface.

As shown in Fig. 2, numerically calculated intensity distributions were in good agreement with the

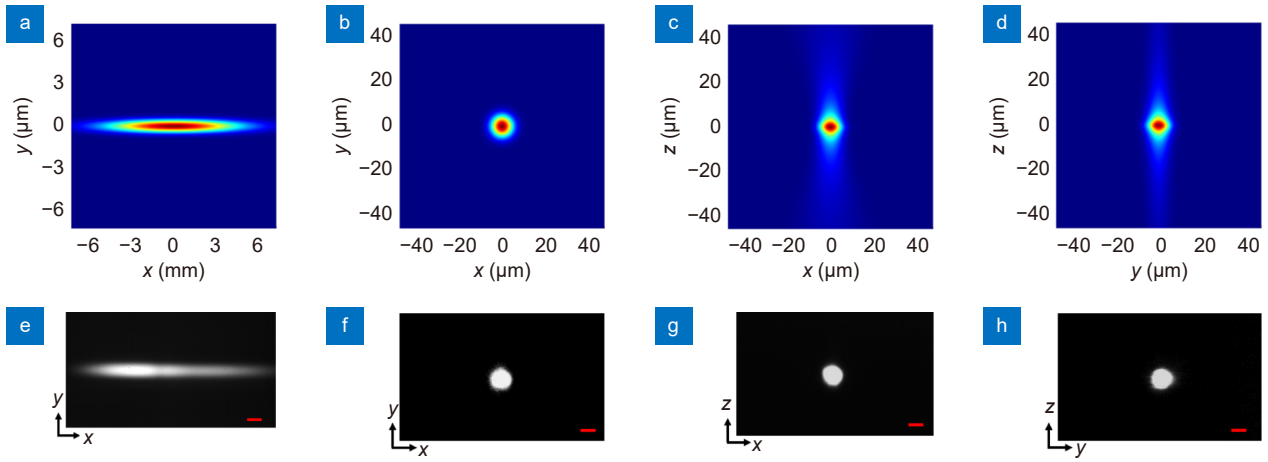

Fig. 2 | (**a**) Numerically calculated and (**e**) experimentally measured laser intensity distributions at the entrance aperture of the objective lens. (**b–d**) Numerically calculated and (**f–h**) experimentally measured intensity distributions near the focus of the objective lens in *XY*, *XZ*-and *YZ* planes, respectively. Scale bars in (**e**) and (**f–h**) are 1 mm and 10 μm, respectively.

experimentally measured results. In the *XY* plane, the intensity distribution at the focus of the objective lens showed a round-shaped profile with a diameter of ~20 μm in Fig. 2(b), indicating the overlapping of different frequency components at the focus of the objective lens. In the *XZ* and *YZ* planes, the cross-sectional profiles are also symmetrical and round-shaped, which were in agreement with the calculated results as shown in Fig. 2(c) and 2(d). Therefore, a nearly perfect 3D symmetrical intensity distribution can be achieved by the SSTF of high-repetition-rate fs laser pulses.

Results and discussion

3D isotropic fabrication resolution

To verify the 3D symmetrical fabrication using the SSTF scheme, a series of lines in glass samples along different directions were inscribed. The pulse energy, repetition rate, writing speed, and processing depth were set at 8 μJ, 10 kHz, 200 μm/s, and 300 μm beneath the glass surface.

Figure 3(a–c) show the schematics of the fabrication procedure with the SSTF scheme along *X*, *Y*, and *Z* directions, respectively. Figure 3(d–f) show the corresponding cross-sectional profiles, whilst Fig. 3(g–i) and 3(j–l) show the corresponding top-view and side-view optical micrographs of the lines, respectively. One can see that all the lines oriented in *X*, *Y*, and *Z* directions are homogeneous and the cross-sectional profiles of the lines are all circular with a diameter of ~16 μm, indicating the capability of 3D isotropic fabrication using the proposed technique. In addition, the cross-sectional profiles in Fig. 2(d–f) were in good agreement with the 3D symmetrical intensity distribution results presented in Fig. 2.

Influence of pulse energy and writing speed

To further investigate the influence of pulse energy on the fabrication resolution in the SSTF scheme, a series of embedded lines with different pulse energies were written in glass. The writing speed and processing depth were 200 μm/s and 300 μm beneath the surface, respectively. The pulse energies varied from 4.7 μJ to 11.0 μJ.

Figure 4(a) and 4(b) present cross-sectional micrographs of fabricated lines with different pulse energies in *XZ* and *YZ* planes, respectively. The pulse energies from left to right were 4.7, 6.2, 7.2, 8.0, 9.5, and 11.0 μJ in Fig. 4(a) and 4(b), respectively. Measured average lateral sizes of cross-sections were 8.3, 13.6, 15.3, 16.3, 20.2, 21.4 μm in the *XZ* plane and 8.3, 13.6, 15.3, 16.3, 20.2, 21.4 μm in the *YZ* plane, while the measured longitudinal sizes were to be 8.3, 13.6, 15.4, 16.5, 20.4, 21.8 μm in the *XZ* plane and 8.3, 13.6, 15.3, 16.3, 20.2, 21.4 μm in the *YZ* plane, respectively. Accordingly, the aspect ratios of lateral and longitudinal sizes with different pulse energies were all ~1. It is obvious that with the increase in pulse energy, the cross-sectional size uniformly increases while maintaining their symmetries in both *XZ* and *YZ* planes (see Figs. 4(a, b) and S1), leading to a 3D tunable isotropic

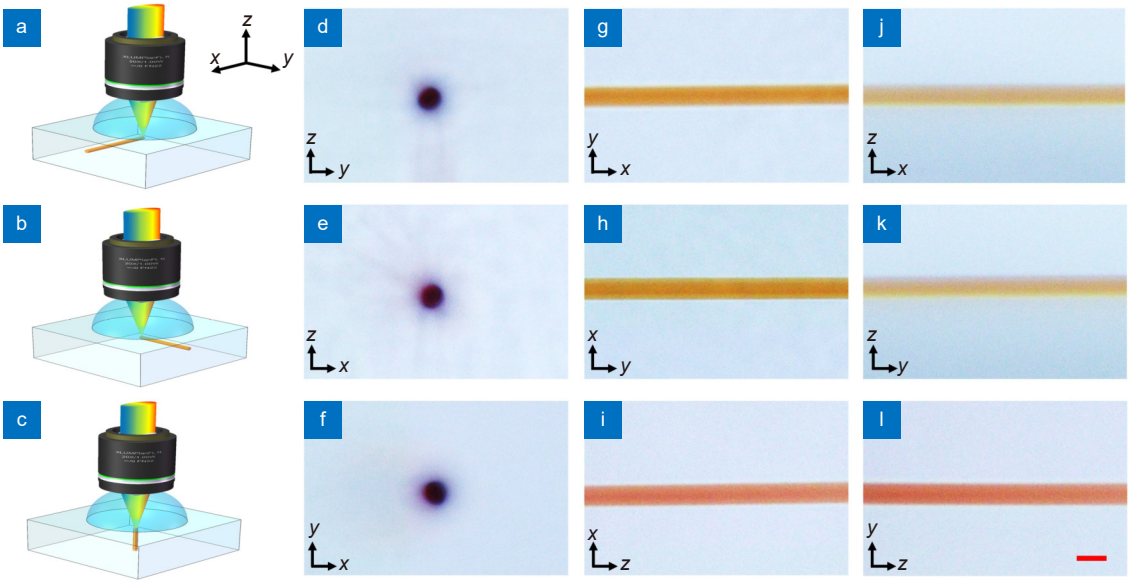

Fig. 3 | Schematics of the fabrication procedure with the SSTF scheme along (**a**) *x*, (**b**) *y*, and (**c**) *z* directions, respectively. (**d–f**) Cross-sectional, (**g–i**) top-view, and (**j–l**) side-view optical micrographs of lines along different directions. The pulse energy and writing speed were 8 μJ and 200 μm/s, respectively. Scale bar: 20 μm.

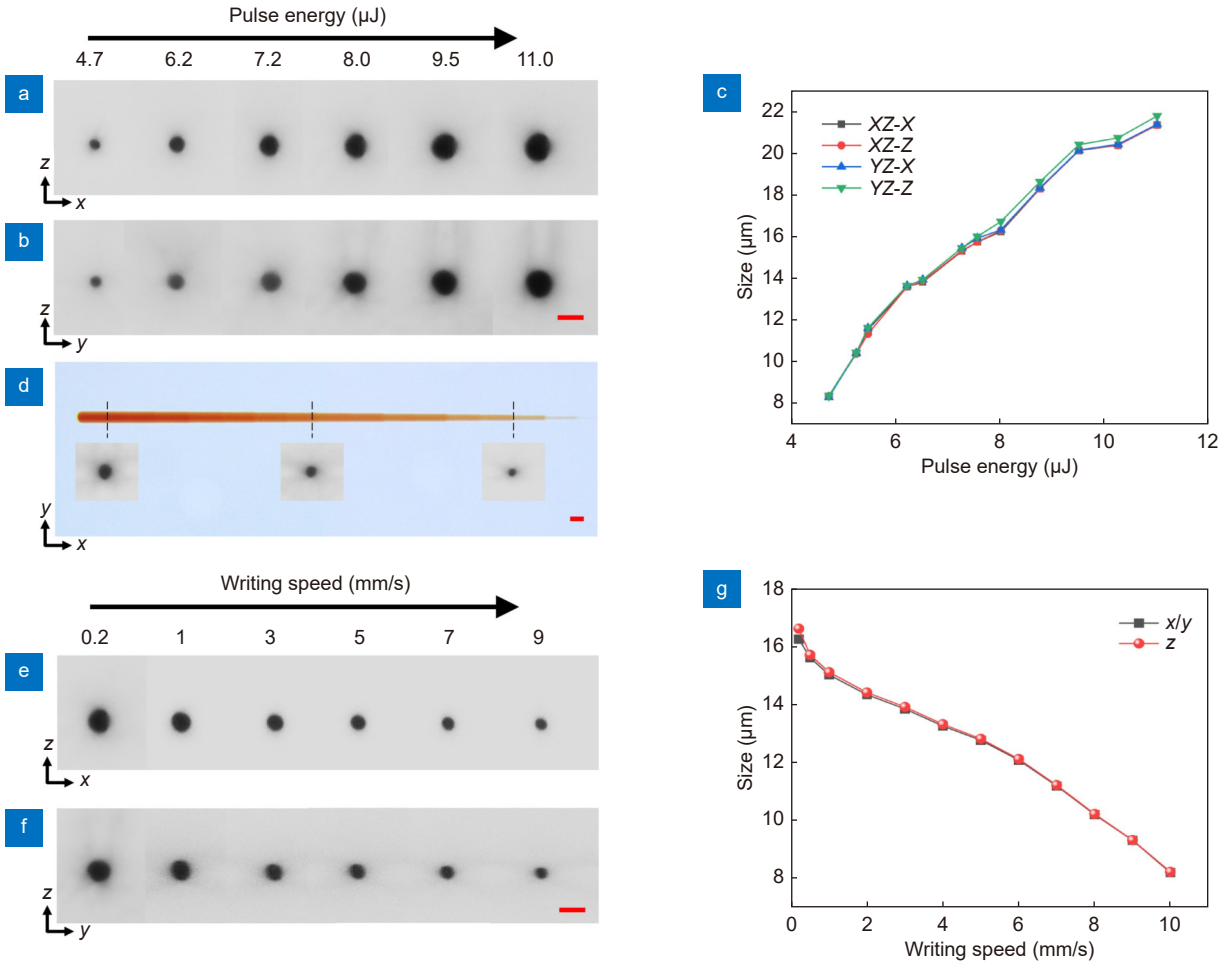

Fig. 4 | The influence of pulse energy and writing speed on the fabrication resolution in the SSTF scheme. Cross-sectional optical micrographs of laser-inscribed lines in the glass along (**a**) *y* and (**b**) *x* directions with different pulse energies ranging from 4.7 μJ to 11.0 μJ. (**c**) Lateral and longitudinal sizes of lines in *XZ* and *YZ* planes versus pulse energies. (**d**) A laser-written line using segmented processing with different pulse energies ranging from 11.0 μJ to 4.7 μJ at a writing speed of 5 μm/s. The insets in (d) are the corresponding cross-sectional view optical micrographs. Cross-sectional optical micrographs of several lines inscribed along (**e**) *y* and (**f**) *x* directions at different writing speeds ranging from 0.2 mm/s to 9 mm/s, pulse energy was set at 8 μJ. (**g**) Lateral and longitudinal resolutions versus writing speeds. Scale bars indicate 20 μm.

resolution ranging from 8 μm to 22 μm.

To quantitatively determine the pulse energy dependence of the fabrication resolution, the lateral and longitudinal sizes of cross sections were plotted as functions of pulse energy in Fig. 4(c). It can be observed that when the pulse energy is in the range of 4.7 to 11 μJ, the lateral and longitudinal sizes in both *XZ* and *YZ* planes are well balanced, and the sizes in both lateral and longitudinal directions show a nearly linear dependence on the pulse energy, the aspect ratios of cross section in both *XZ* and *YZ* planes are all about 1.

To demonstrate the tunability of fabrication resolution, we fabricated a line using segmented processing with different pulse energies and a writing speed of 5 μm/s (see Fig. 4(d)). The pulse energies varied from 11 μJ to 4.7 μJ from left to right with a segmented distance of 50 μm. The insets in Fig. 4(d) show the cross-sections of the corresponding locations. This result revealed that 3D isotropic fabrication resolution could be continuously tuned with the variation of the pulse energy.

To investigate the influence of writing speed on the fabrication resolution, a series of embedded lines at different writing speeds were also inscribed in the glass. The pulse energy and processing depth were set at 8 μJ and 300 μm beneath the surface, respectively. The writing speed varied from 0.2 mm/s to 9 mm/s. Figure 4(e) and 4(f) present cross-sectional micrographs of the fabricated lines in the *XZ* and *YZ* planes, respectively. The writing speeds from left to right are 0.2, 1, 3, 5, 7, and 9 mm/s in both Fig. 4(e) and 4(f). When the writing speed changed, the measured lateral sizes were 16.3, 15.0, 13.8, 12.7, 11.2, and 9.2 μm and the axial sizes were 16.6, 15.1,

13.9, 12.8, 11.2, and 9.2 μm, respectively. The aspect ratios of lateral and axial sizes at different writing speeds were all ~1. With increasing writing speed, the cross-sectional sizes gradually decreased in the SSTF scheme, and all cross-sectional shapes remain circular in both *XZ* and *YZ* planes at different writing speeds, resulting in a 3D tunable isotropic fabrication resolution ranging from 9 μm to 16 μm (see Figs. 4(e, f) and S2). As shown in Fig. 4(g), the cross-sectional size showed a nearly negative linear dependence on the writing speed.

Influence of processing depth

To investigate the influence of processing depth on the fabrication resolution with the SSTF scheme, a series of lines at different depths and pulse energies were inscribed in glass as illustrated in Fig. 5(a). All the lines were written at a speed of 200 μm/s.

Figure 5(b) and 5(c) present the cross-sectional optical micrographs of lines fabricated at different depths in *YZ* and *XZ* planes, respectively. The pulse energies from left to right were 8.7, 8.0, 7.2, 6.2, and 5.4 μJ, and the depths of the focal position were 160, 480, 800, 1120, and 1440 μm, as indicated in Fig. 5(b) and 5(c). It is obvious that all the cross-sectional profiles in both *XZ* and *YZ* planes were symmetrical and round-shaped, and the lateral and longitudinal sizes of cross-sections were almost unchanged at different depths (see Figs. 5(b, c) and S3), which means that the fabrication resolutions in both *XZ* and *YZ* planes were insensitive to the depth of the focal position in the SSTF scheme. Figur 5(d) further confirmed that the lateral and longitudinal sizes were well balanced at different depths in both *XZ* and *YZ* planes when the processing depth was less than 800 μm, and the corresponding aspect ratios of cross-sectional shapes were 1. When the depth was beyond 800 μm, although the lateral and longitudinal sizes were not balanced, the maximum aspect ratio was only 1.1.

Influence of spherical aberration

To investigate the effect of spherical aberration on the fabrication resolution, we first wrote lines with different pulse energies when the water-immersion objective lens was not immersed in water, as illustrated in Fig. 6(a). The fabrication parameters were almost the same as those in Fig. 4(a) and 4(b). The writing speed and the processing depth were 200 μm/s and 300 μm beneath the surface, respectively. The pulse energy varied from 4.75 μJ to 22.8 μJ.

Figure 6(b) and 6(c) present the cross-sectional optical micrographs of lines fabricated at the increasing pulse energy in *XZ* and *YZ* planes when the objective lens is not immersed in water. It should be noted that compared with the results in Fig. 4(a) and 4(b), there was no visible modified area at the same pulse energy. Only when the pulse energy increased to 14.8 μJ, the lines could be fabricated in the SSTF scheme, which means that the fabrication of lines needs more laser intensity when the objective lens was not immersed in water than

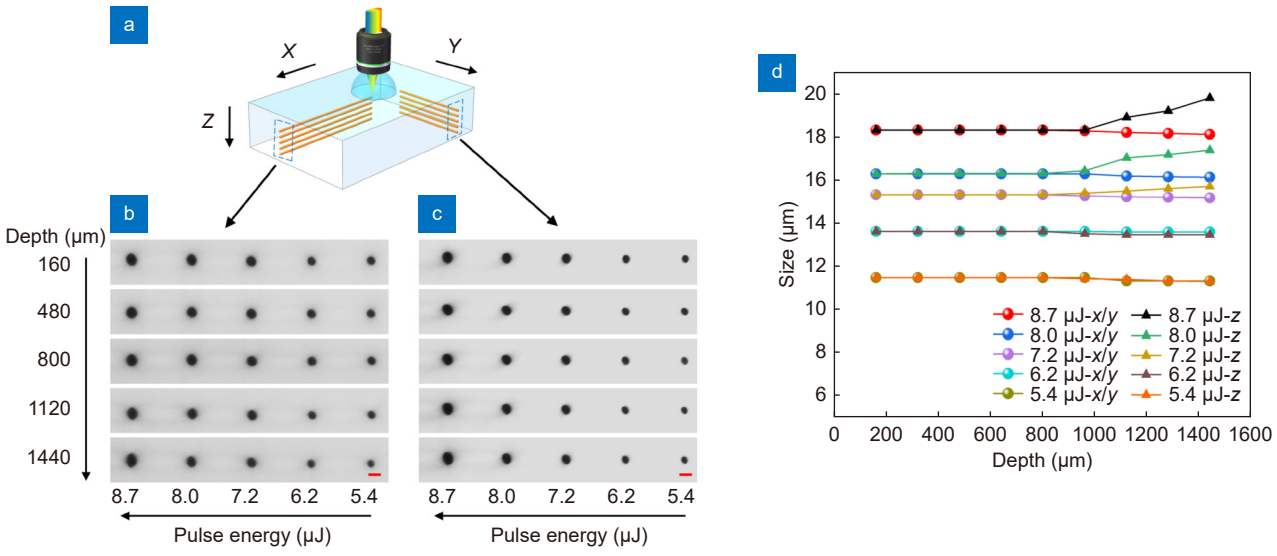

Fig. 5 | The influence of processing depth on the fabrication resolution in the SSTF scheme. (**a**) Schematic of inscribing lines in glass at different depths along the *X* and *Y* directions. Cross-sectional optical micrographs of the lines written along the (**b**) *X* and (**c**) *Y* directions, respectively. (**d**) The lateral and longitudinal resolutions versus depth. Scale bar: 20 μm.

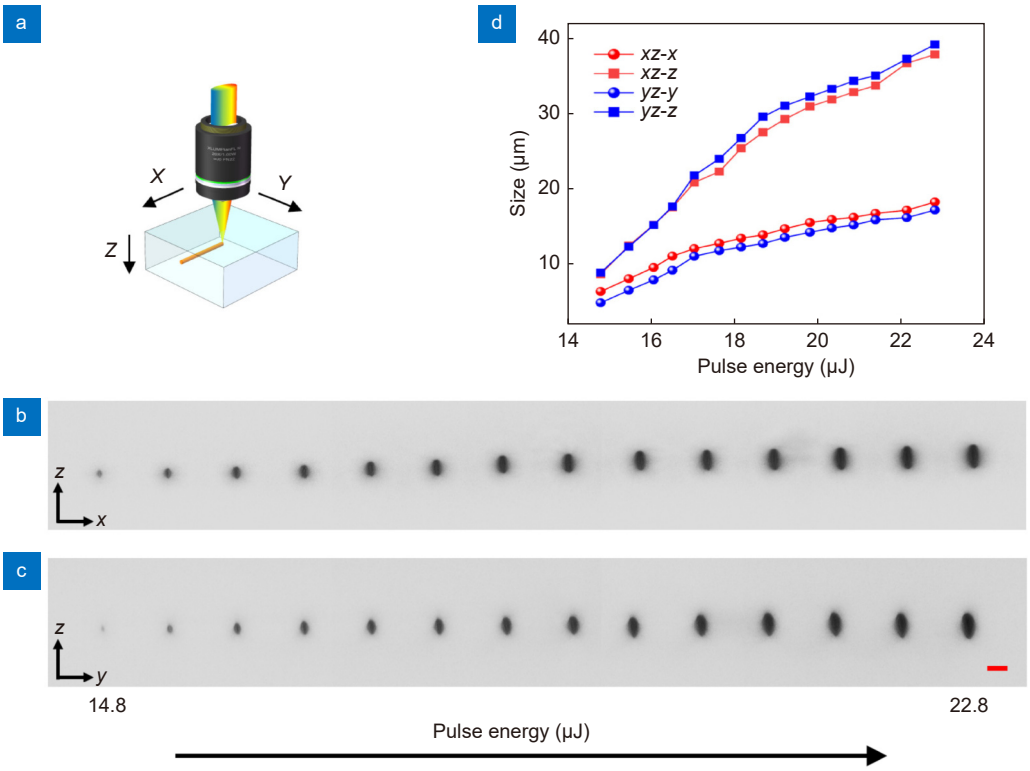

Fig. 6 | (**a**) Schematic of laser-inscribed lines in the glass when the objective lens was not immersed in water. Cross-sectional optical micrographs of the lines along (**b**) *Y* and (**c**) *X* directions at different pulse energies. The pulse energies varied from 14.8 μJ to 22.8 μJ from left to right in both (b) and (c). (**d**) The lateral and longitudinal sizes in *XZ* and *YZ* planes versus pulse energies. Scale bar: 20 μm.

that immersed in water. This phenomenon could be explained by the fact that different frequency components were not overlapped well due to the effects of the spherical aberration in the SSTF scheme.

As shown in Fig. 6(d), the lateral and longitudinal sizes showed a nearly linear dependence on the pulse energy, however, the ratios of cross sections in both *XZ* and *YZ* planes are more than 1.5, which revealed that 3D isotropic fabrication resolution could not be achieved in SSTF scheme due to the effects of spherical aberrations.

Moreover, it was found that with a conventional focusing (CF) scheme under the same fabrication parameters, it was impossible to obtain a 3D isotropic resolution (see Fig. S4).

Demonstration of 3D isotropic fabrication

To demonstrate the unique capability of 3D isotropic fabrication in glass with the SSTF scheme, four helical lines with different pulse energies were inscribed from the rear surface to the front surface of 1.6 mm thick glass. Figure 7(a) and 7(e) show the cross-sectional view and top-view optical micrographs of the fabricated helical lines. The writing speed was fixed at 200 μm/s and the pulse energies from left to right were 9.5, 8.0, 7.2, and 6.2 μJ, respectively. The helical lines with coil diameters of 200 μm in the *XY* plane and the *Z*-direction pitches of 200 μm were written. The measured widths of helical lines from left to right were 20.2, 16.3, 15.3, and 13.6 μm (see Fig. 7(a) and 7(b)), respectively. As shown in Fig. 7(c, d, g), all the helical lines were homogeneous not only at different depths but also in the *XY* planes, which further provided evidence of the 3D isotropic fabrication resolution with the SSTF scheme. Compared with conventional 3D FLDW, the SSTF scheme provides a 3D tunable and depth-insensitive 3D isotropic fabrication resolution.

3D homogeneous microchannel fabrication

To demonstrate the capability for fabricating spatially homogeneous microfluidic structures, SSTF FLDW-assisted etching was performed as illustrated in Fig. 8(a), the fabrication procedure consists of three main steps: (I) SSTF fs laser direct writing; (II) thermal annealing; (III) chemical etching. 10% hydrofluoric (HF) solution was employed for the selective removal of the laser-modified lines to form glass microchannels. A meandering cooling structure microchannel was firstly fabricated embedded in glass with a depth of 100 μm. To ensure the etching

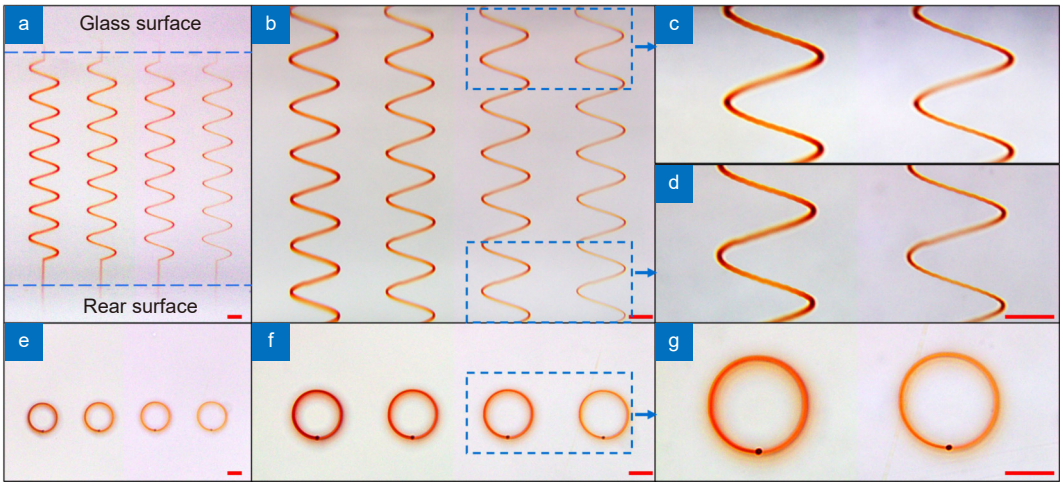

Fig. 7 | (**a**–**d**) Cross-sectional view and (**e**–**g**) top-view optical micrographs of helical lines written throughout 1.6 mm thick glass at different pulse energies with the SSTF scheme. The writing speed was set at 200 μm/s, and the pulse energies from left to right were 9.5, 8.0, 7.2, and 6.2 μJ, respectively. (**c**) and (d) Enlarged images of (**b**) at different depths. (g) Enlarged image in (**f**). Scale bar: 100 μm.

homogeneity of the channel, a series of extra-access ports distributed along the whole channel with a spacing of 100 μm was adopted. The writing speed and the pulse energy were 200 μm/s and 6.2 μJ, respectively. Figure 8(b) shows the optical micrographs of the channel structures after laser irradiation followed by thermal annealing, the measured width of the line was ~13.6 μm. After thermal annealing, the sample was immersed in a 10% HF solution under an ultrasonic bath for 15 min at room temperature. Figure 8(c) and 8(d) show the optical micrograph of the etched microchannel and its enlarged image. One can see that the whole channel was uniform and its width was almost unchanged along the channel (total length: ~50000 μm) (see the inset of Fig. 8(d)), indicating the ability to prepare large-scale and highly uniform functional microstructures in glass using SSTF FLDW assisted etching. For instance, it may also further promote the performance of fs laser-fabricated optofluidic waveguides in glass[38].

To further demonstrate the powerful capability of the fabrication of 3D complicated microfluidic structures by SSTF FLDW assisted etching, a 3D multi-layer microfluidic network structure with a size of 3.75 mm × 3.75 mm × 0.5 mm was fabricated, as shown in the inset of Fig. 8(g). The writing speed and pulse energy were 5 mm/s and 8 μJ, respectively. Figure 8(e, h, k) show the optical micrographs of the laser-written network structure in *XY*, *XZ*, and *YZ* planes after laser irradiation followed by thermal annealing. The spacings between lines in the *XY* plane and in both *XZ* and *YZ* planes were 150 μm and 120 μm, respectively. The widths of all lines are ~12.7 μm. Then, the sample was etched in a 10% HF solution under an ultrasonic bath for 50 min. Figure 8(f, i, l) show the optical micrographs of the etched network structure in *XY*, *XZ*, and *YZ* planes. As shown in Fig. 8(g, j, m), all etched channels oriented in *X*, *Y*, and *Z* directions exhibited a nearly circular cross-section with a width of ~30 μm, revealing the capability for the fabrication of 3D large-scale and uniform complicated microfluidic structures using the proposed technique.

In addition, four helical hollow microchannels in 500 μm thick glass were also fabricated. The pulse energy and the writing speed were 6.2 μJ and 200 μm/s, respectively. Figure 8(n, q) show the top-view and side-view optical micrographs of helical lines after FLDW followed by thermal annealing. The diameter and pitch of coils were all 150 μm and the helical lines were homogeneous with a width of 13.6 μm. Then, after the etching of 10% HF solution under an ultrasonic bath for 45 min, the embedded helical microchannels with a width of ~30 μm and a coil diameter of 150 μm were fabricated from the front surface to the rear surface, as shown in Fig. 8(o, r). As presented in Fig. 8(p, s), although there was a small variation along these two channels, the whole helical microchannels were relatively uniform.

Conclusions

In conclusion, we have successfully applied the SSTF technique to a high-repetition-rate fs fiber laser system and demonstrated the capability of the SSTF technique for 3D isotropic microfabrication with a tunable resolution in the glass. To solve the problem of insufficient

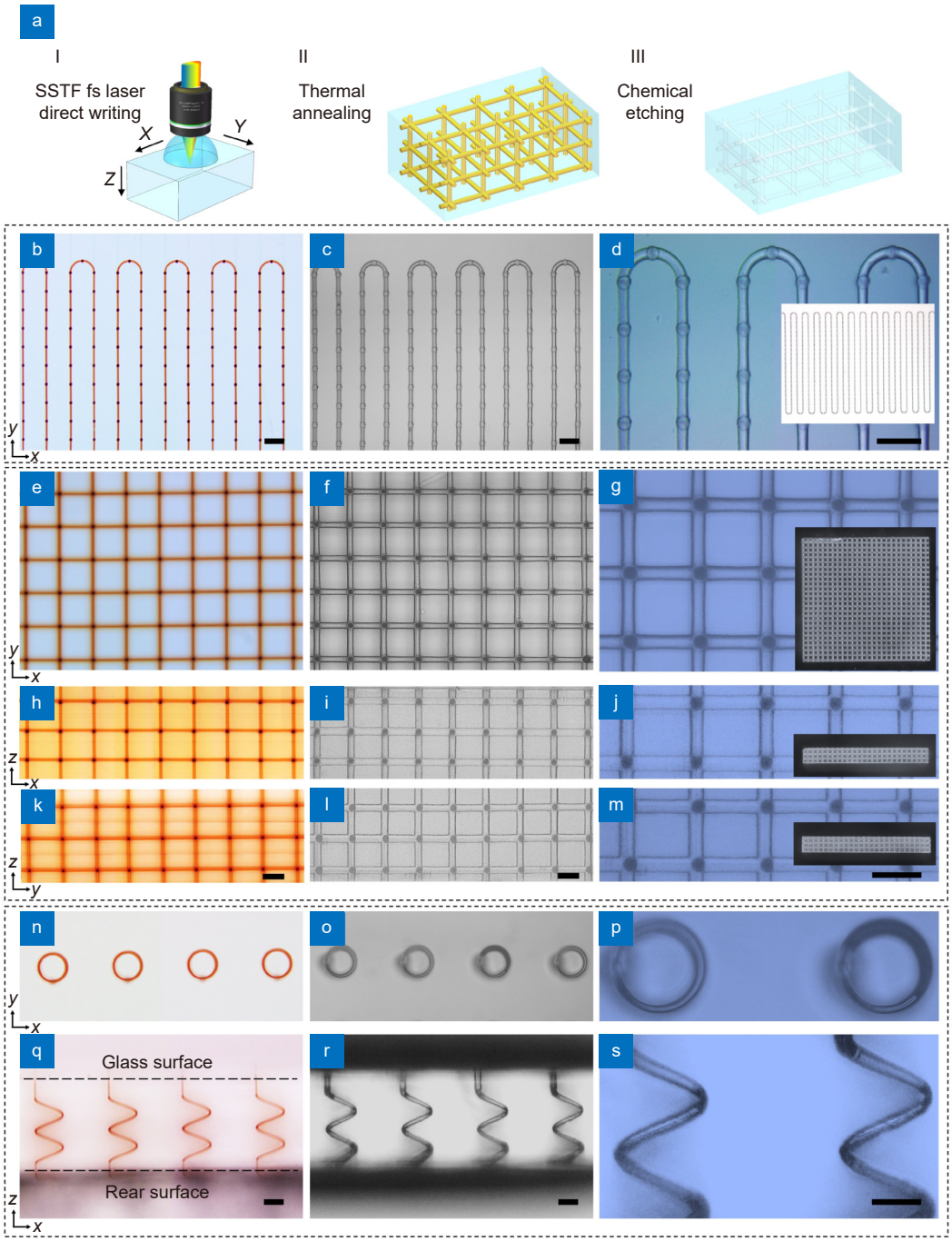

Fig. 8 | (**a**) Schematic of the fabrication procedure for 3D microchannel structures in glass by a combination of SSTF FLDW assisted etching, which consists of three main steps: (I) SSTF fs laser direct writing; (II) thermal annealing; (III) chemical etching. (**b**–**d**) A meandering cooling structure microchannel. Optical micrographs of the channel structure (b) after FLDW followed by thermal annealing and (c) after etching. (d) An enlarged image in (c). (**e**–**m**) A 3D multilayer microchannel network structure. Optical micrographs of the 3D network structure (e, h, k) after FLDW followed by thermal annealing and after etching in *XY*, *XZ*, and *YZ* planes. (**g**, **j**, **m**) were enlarged images in (**f**, **i**, **l**), respectively. (**n**–**s**) 3D helical microchannel structures. The top-view (**n**,**o**) and side-view (**q**,**r**) optical micrographs of the 3D helical lines fabricated after FLDW followed by thermal annealing and after etching. (**p**) and (**s**) are enlarged images in (o) and (r), respectively. The insets in (d, g, j, m) are photographs of the microchannel structures. Scale bar: 100 μm.

pulse compensation for a narrow-bandwidth fiber laser source in the SSTF scheme, we have built a pulse stretcher outside the laser source and confirmed its validity. We have theoretically and experimentally demonstrated that 3D symmetrical intensity distributions near the laser focus can be achieved with the SSTF scheme, respectively. Meanwhile, 3D tunable isotropic fabrication resolution ranging from 8 μm to 22 μm in glass can be achieved by varying the pulse energy of the fs laser, which remains a challenge for the conventional focusing scheme. We also systematically investigated the influences of writing speed, processing depth, and spherical aberration on the fabrication resolution in the SSTF scheme. The cross-sectional size exhibits a nearly linear dependence on the writing speed due to the modulation of exposure doses. The fabrication resolution is insensitive to the depth of the focal position at a certain degree and the rational control of the spherical aberration is of importance for maintaining the 3D isotropic fabrication resolution. This proposed technique overcomes the problem of asymmetric resolution in the conventional FLDW process and extends the processing window of 3D isotropic fabrication resolution, which will be beneficial for developing 3D high-uniform microstructures and novel functional microdevices.

References

1. Davis KM, Miura K, Sugimoto N, Hirao K. Writing waveguides in glass with a femtosecond laser. *Opt Lett* **21**, 1729–1731 (1996).
2. Marcinkevičius A, Juodkazis S, Watanabe M, Miwa M, Matsuo S et al. Femtosecond laser-assisted three-dimensional microfabrication in silica. *Opt Lett* **26**, 277–279 (2001).
3. Kawata S, Sun HB, Tanaka T, Takada K. Finer features for functional microdevices. *Nature* **412**, 697–698 (2001).
4. Cheng Y, Sugioka K, Midorikawa K. Microfluidic laser embedded in glass by three-dimensional femtosecond laser microprocessing. *Opt Lett* **29**, 2007–2009 (2004).
5. Kowalevicz AM, Sharma V, Ippen EP, Fujimoto JG, Minoshima K. Three-dimensional photonic devices fabricated in glass by use of a femtosecond laser oscillator. *Opt Lett* **30**, 1060–1062 (2005).
6. Sugioka K, Cheng Y, Midorikawa K. Three-dimensional micromachining of glass using femtosecond laser for lab-on-a-chip device manufacture. *Appl Phys A* **81**, 1–10 (2005).
7. Sugioka K, Cheng Y. Ultrafast lasers—reliable tools for advanced materials processing. *Light Sci Appl* **3**, e149 (2014).
8. Malinauskas M, Žukauskas A, Hasegawa S, Hayasaki Y, Mizeikis V et al. Ultrafast laser processing of materials: from science to industry. *Light Sci Appl* **5**, e16133 (2016).
9. Xu J, Li XL, Zhong Y, Qi J, Wang ZH et al. Glass-channel molding assisted 3D printing of metallic microstructures enabled by femtosecond laser internal processing and microfluidic electroless plating. *Adv Mater Technol* **3**, 1800372 (2018).
10. Lin ZJ, Xu J, Song YP, Li XL, Wang P et al. Freeform microfluidic networks encapsulated in laser‐printed 3D macroscale glass objects. *Adv Mater Technol* **5**, 1900989 (2020).
11. Liu ZM, Xu J, Lin ZJ, Qi J, Li XL et al. Fabrication of single-mode circular optofluidic waveguides in fused silica using femtosecond laser microfabrication. *Opt Laser Technol* **141**, 107118 (2021).
12. Jia YC, Wang SX, Chen F. Femtosecond laser direct writing of flexibly configured waveguide geometries in optical crystals: fabrication and application. *Opto-Electron Adv* **3**, 190042 (2020).
13. Tan DZ, Wang Z, Xu BB, Qiu JR. Photonic circuits written by femtosecond laser in glass: improved fabrication and recent progress in photonic devices. *Adv Photon* **3**, 024002 (2021).
14. Wolf A, Dostovalov A, Bronnikov K, Skvortsov M, Wabnitz S et al. Advances in femtosecond laser direct writing of fiber Bragg gratings in multicore fibers: technology, sensor and laser applications. *Opto-Electron Adv* **5**, 210055 (2022).
15. Sugioka K, Xu J, Wu D, Hanada Y, Wang ZK et al. Femtosecond laser 3D micromachining: a powerful tool for the fabrication of microfluidic, optofluidic, and electrofluidic devices based on glass. *Lab Chip* **14**, 3447–3458 (2014).
16. Serien D, Sugioka K. Fabrication of three-dimensional proteinaceous micro- and nano-structures by femtosecond laser cross-linking. *Opto-Electron Adv* **1**, 180008 (2018).
17. Cheng Y, Sugioka K, Midorikawa K, Masuda M, Toyoda K et al. Control of the cross-sectional shape of a hollow microchannel embedded in photostructurable glass by use of a femtosecond laser. *Opt Lett* **28**, 55–57 (2003).
18. Ams M, Marshall GD, Spence DJ, Withford MJ. Slit beam shaping method for femtosecond laser direct-write fabrication of symmetric waveguides in bulk glasses. *Opt Express* **13**, 5676–5681 (2005).
19. Osellame R, Taccheo S, Marangoni M, Ramponi R, Laporta P et al. Femtosecond writing of active optical waveguides with astigmatically shaped beams. *J Opt Soc Am B* **20**, 1559–1567 (2003).
20. Sugioka K, Cheng Y, Midorikawa K, Takase F, Takai H. Femtosecond laser microprocessing with three-dimensionally isotropic spatial resolution using crossed-beam irradiation. *Opt Lett* **31**, 208–210 (2006).
21. Vishnubhatla KC, Bellini N, Ramponi R, Cerullo G, Osellame R. Shape control of microchannels fabricated in fused silica by femtosecond laser irradiation and chemical etching. *Opt Express* **17**, 8685–8695 (2009).
22. Zhu GH, van Howe J, Durst M, Zipfel W, Xu C. Simultaneous spatial and temporal focusing of femtosecond pulses. *Opt Express* **13**, 2153–2159 (2005).
23. Oron D, Tal E, Silberberg Y. Scanningless depth-resolved microscopy. *Opt Express* **13**, 1468–1476 (2005).
24. He F, Xu H, Cheng Y, Ni JL, Xiong H et al. Fabrication of microfluidic channels with a circular cross section using spatiotemporally focused femtosecond laser pulses. *Opt Lett* **35**, 1106–1108 (2010).
25. Vitek DN, Adams DE, Johnson A, Tsai PS, Backus S et al. Temporally focused femtosecond laser pulses for low numerical aperture micromachining through optically transparent materials. *Opt Express* **18**, 18086–18094 (2010).
26. He F, Cheng Y, Lin JT, Ni JL, Xu ZZ et al. Independent control of aspect ratios in the axial and lateral cross sections of a focal spot for three-dimensional femtosecond laser micromachining.

New J Phys **13**, 083014 (2011).
27. Kammel R, Ackermann R, Thomas J, Götte J, Skupin S et al. Enhancing precision in fs-laser material processing by simultaneous spatial and temporal focusing. *Light Sci Appl* **3**, e169 (2014).
28. Zeng B, Chu W, Gao H, Liu WW, Li GH et al. Enhancement of peak intensity in a filament core with spatiotemporally focused femtosecond laser pulses. *Phys Rev A* **84**, 063819 (2011).
29. He F, Zeng B, Chu W, Ni JL, Sugioka K et al. Characterization and control of peak intensity distribution at the focus of a spatiotemporally focused femtosecond laser beam. *Opt Express* **22**, 9734–9748 (2014).
30. Tan YX, Wang ZH, Chu W, Liao Y, Qiao LL et al. High-throughput in-volume processing in glass with isotropic spatial resolutions in three dimensions. *Opt Mater Express* **6**, 3787–3793 (2016).
31. Tan YX, Chu W, Wang P, Li WB, Qi J et al. High-throughput multi-resolution three dimensional laser printing. *Phys Scr* **94**, 015501 (2019).
32. Sun BS, Salter PS, Roider C, Jesacher A, Strauss J et al. Four-dimensional light shaping: manipulating ultrafast spatiotemporal foci in space and time. *Light Sci Appl* **7**, 17117 (2018).
33. Quinoman P, Chimier B, Duchateau G. Theoretical study of spatiotemporal focusing for in-bulk laser structuring of dielectrics. *J Opt Soc Am B* **39**, 166–176 (2022).
34. Cheng WB, Wang ZH, Liu XL, Cheng Y, Polynkin P. Microexplosions in bulk sapphire driven by simultaneously spatially and temporally focused femtosecond laser beams. *Opt Lett* **48**, 751–754 (2023).
35. Hansen WW, Janson SW, Helvajian H. Direct-write UV-laser microfabrication of 3D structures in lithium-aluminosilicate glass. *Proc SPIE* **2991**, 104–112 (1997).
36. Cheng Y, Sugioka K, Masuda M, Shihoyama K, Toyoda K et al. Optical gratings embedded in photosensitive glass by photochemical reaction using a femtosecond laser. *Opt Express* **11**, 1809–1816 (2003).
37. Martinez O. 3000 times grating compressor with positive group velocity dispersion: application to fiber compensation in 1.3-1.6 μm region. *IEEE J Quantum Electron* **23**, 59–64 (1987).
38. Yu JP, Xu J, Dong QN, Qi J, Chen JF et al. Low-loss optofluidic waveguides in fused silica enabled by spatially shaped femtosecond laser assisted etching combined with carbon dioxide laser irradiation. *Opt Laser Technol* **158**, 108889 (2023).

Acknowledgements

This work was supported by the National Key Research and Development Program of China (2019YFA0705000, 2022YFA1404800); National Natural Science Foundation of China (12004221, 12174107, 12192254, 11734009, 12192251, 92250304, 11974218); Postdoctoral Innovation Talents Support Program of Shandong Province (No. SDBX2019005); Science and Technology Commission of Shanghai Municipality (21DZ1101500); Local science and technology development project of the central government (YDZX20203700001766); Shanghai Municipal Science and Technology Major Project; Natural Science Foundation of Shandong Province (ZR2021ZD02).

Author contributions

Y. X. Tan, H. T. Lv, A. D. Zhang, Y. P. Song, J. P. Yu, W. Chen, Y. X. Wan, Z. X. Liu, Z. H. Liu, J. Qi performed the numerical simulations and conducted the experiments, Y. X. Tan, J. Xu, and H. T. Lv, wrote the manuscript, J. Xu and Y. Cheng conceived the idea, J. Xu, Y. J. Cai, and Y. Cheng supervised the work, All the authors discussed and analyzed the results and commented on the manuscript at all stages.

Competing interests

The authors declare no competing financial interests.

Supplementary information

The Supplementary information is available at https://doi.org/10.29026/oea.2023.230066